Flow-induced vibrations of elastically-coupled tandem cylinders: Supplementary Material

Gaurav Sharma, Rajneesh Bhardwaj*
Department of Mechanical Engineering,
Indian Institute of Technology Bombay, Mumbai 400076, India
*Corresponding author: rajneesh.bhardwaj@iitb.ac.in

S1 Computation methodology

The coupled fluid-solid equations (Eq.(2.1) - Eq.(2.3)) are solved using the sharp-interface immersed boundary method in $2D$. The method has been described in detail by Mittal *et al.* (2008) and has been briefly presented here. The fluid flow is solved using the fractional step method on a two-dimensional non-uniform Cartesian grid. The equations are discretized in space using the cell-centered, collocated arrangement of pressure and velocity using the finite difference method. The convective and diffusive terms in Eq.(2.2) are discretized using the second-order central difference method. The time marching of the advection-diffusion equation is performed using the Crank-Nicholson scheme to obtain an intermediate velocity field. The pressure Poisson equation is solved using a geometric multigrid method. Finally, the velocity field is updated by enforcing mass conservation (Eq.(2.1)) in the flow domain.

The coupled structural vibration equations (Eq.(2.3)) are discretized using the first-order Euler's method. While an uncoupled elastically-mounted systems can be solved for structural accelerations sequentially, the two equations are coupled in this case, and the motion of the two cylinders will influence each other. Therefore, the two equations are solved simultaneously, as shown in Eq. (S1). The velocity and displacement are obtained using the first and second order time integral of acceleration.

$$\begin{bmatrix} \ddot{y}_1 \\ \ddot{y}_2 \end{bmatrix}^{n+1} = \begin{bmatrix} 4F_{T1}/\pi m \\ 4F_{T2}/\pi m \end{bmatrix}^{n} - \begin{bmatrix} k_1 + k_2 & -k_2 \\ -k_2 & k_2 + k_3 \end{bmatrix} \begin{bmatrix} y_1 \\ y_2 \end{bmatrix}^{n} \tag{S1}$$

where superscript n denotes n^{th} time step. The flow domain is solved using the Eulerian description of the pressure and velocity field, and is coupled with the Lagrangian description of the solid surface through the immersed boundary. The unstructured triangular mesh on the structure surface is used to identify the immersed boundaries. These immersed boundaries are treated as sharp interfaces, and the velocity at ghost nodes (nodes near immersed boundary) is interpolated to impose the boundary condition at the interface (citeMittal2008). The surface forces are calculated at the immersed boundary and passed to the structure for updating the location of the interface, and the flow field is updated accordingly. A cut-cell method (Seo & Mittal (2011)) is used to treat spurious pressure oscillations at the sharp-interface immersed boundary. The FSI solver is second-order accurate in space and time for the fluid domain and first-order accurate in time for the structural domain. A detailed description of the sharp-interface immersed boundary method can be found in Mittal *et al.* (2008) and the FIV solver can be found in Garg *et al.* (2018).

S2 Domain and grid size independence tests

Figure S1 shows the domain and grid independence tests performed for cylinder displacements of upstream (y_1) and downstream (y_2) cylinders for the configuration shown in Figure 1 of the main manuscript. The elastically coupled system with $k_1 = 0.1, k_2 = 0.324, k_3 = 0$ is considered for $m = 10$ cylinders placed at $G = 3$ in an $Re = 100$ flow. The above configuration corresponds to $U_R = 7.5$ of Case 3. This particular case is considered as it shows significantly high amplitude vibrations for both the cylinders and corresponds to maximum blockage ($\sim 6.7\%$). The domain

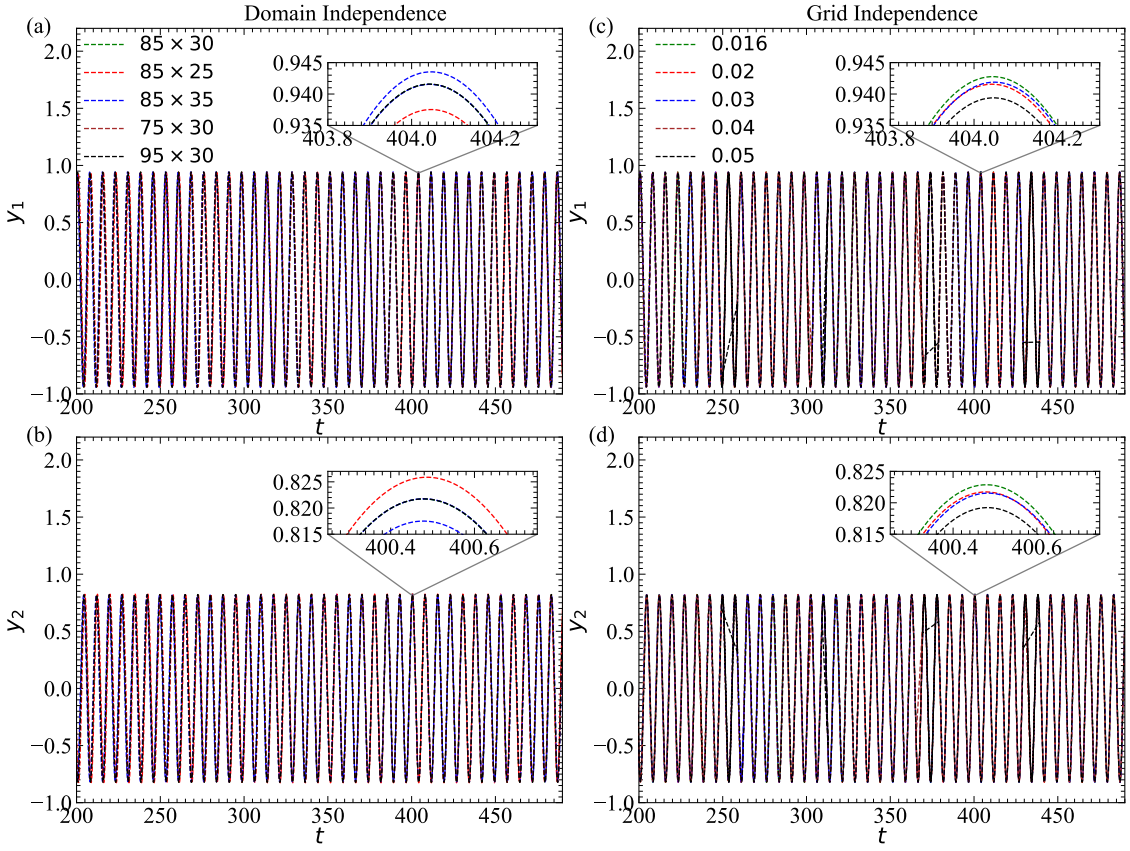

Figure S1: Convergence of domain for the (a) upstream and (b) downstream cylinder, and grid for (c) upstream and (d) downstream cylinder are plotted. Insets indicate domain and grid size independence obtained at 85×30 and 0.02, respectively.

size independence studies (see Figure S1(a) and (b)) are performed using five domains with varying domain sizes from 75 to 95 in x, and from 25 to 35 in y direction, using a minimum grid size of $\Delta x = \Delta y = 0.02$ and time step size $\Delta t = 0.01$. The CFL number is always maintained well below 1. Figure S1(a) and (b) shows the variation of the amplitudes y_1 and y_2 within $\sim 1\%$ error bounds. Therefore, the domain size of 85×30 is utilized for all the subsequent simulations.

The grid size independence tests (see Figure S1(c) and (d)) are performed by varying the minimum grid size from 0.05 to 0.01 on an 85 domain using time step size $\Delta t = 0.01$ ($\Delta t = 0.005$ for 0.01 grid size). A uniform Cartesian fine grid is maintained close to the cylinders, with square cells for enhanced accuracy. The grid is gradually coarsened in the regions away from the two

cylinders. The CFL number is always maintained well below 1. The variation of the amplitudes y_1 and y_2 is within $\sim 1\%$ error bounds for a grid size of 0.02.

S3 Code verification tests

The FSI solver has been validated for various benchmark studies (Mittal *et al.* (2008)). In our previous studies, flow across stationary cylinders (Sharma *et al.* (2022*b*)), FIV of isolated cylinders (Sharma *et al.* (2022*a*)), and FIV of independent tandem cylinders (Garg *et al.* (2020)) have been verified against benchmark data. However, the present study includes elastic coupling between the two cylinders in tandem. Furthermore, the solver has been extended to include the elastic coupling between the cylinders. Therefore, it is only appropriate to supplement the present verification study with the past FIV studies of elastically coupled cylinders. We verify the present solver implementation using the FIV response data reported by Ding *et al.* (2020) for the elastically coupled cylinders in a side-by-side configuration. Figure S2 shows the A_{max} amplitude response for the considered three cases, using Strouhal frequency (a) close to the first natural frequency, (b) between the two natural frequencies, and (c) close to the second natural frequency of the structural system. The A_{max} response simulated using the present solver shows good agreement with the results of Ding *et al.* (2020) for all three cases. Deviations in A_{max} values of the present study with respect to Ding *et al.* (2020) can be attributed to the differences in the numerical methods and computational grids.

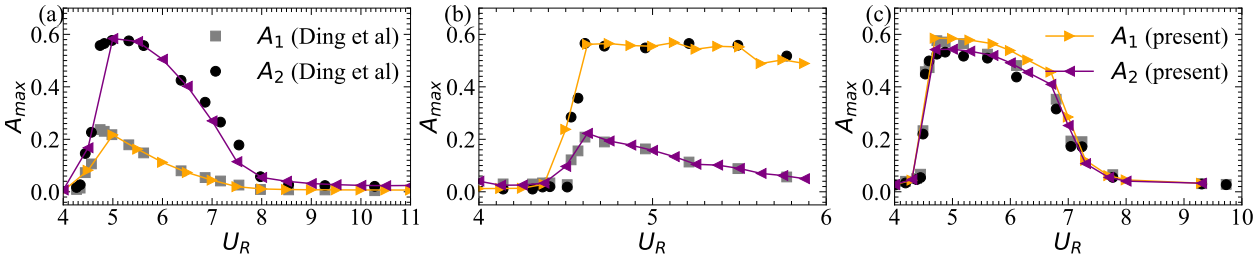

Figure S2: The FIV response of two elastically coupled cylinders in side-by-side configuration is compared for the present solver with Ding *et al.* (2020), using the maximum displacement amplitude A_{max} of the cylinders. A_1 (lower cylinder) and A_2 (upper cylinder) of the present study reasonably agree with Ding *et al.* (2020) for their three cases corresponding to (a) $f_{n1} \sim St_0$, (b) $f_{n1} < St_0 < f_{n2}$, and (c) $f_{n2} \sim St_0$

S4 Modal analysis

As shown in the main manuscript Eq 2.3, the structural vibration equation for the elastically coupled cylinder system, shown in Figure 1 in the paper, is as follows,

$$\begin{bmatrix} 1 & 0 \\ 0 & 1 \end{bmatrix} \begin{bmatrix} \ddot{y}_1 \\ \ddot{y}_2 \end{bmatrix} + \begin{bmatrix} k_1 + k_2 & -k_2 \\ -k_2 & k_2 + k_3 \end{bmatrix} \begin{bmatrix} y_1 \\ y_2 \end{bmatrix} = \begin{bmatrix} 4F_{T1}/\pi m \\ 4F_{T2}/\pi m \end{bmatrix} \tag{S2}$$

or

$$\boldsymbol{M}\ddot{\boldsymbol{x}} + \boldsymbol{K}\boldsymbol{x} = \boldsymbol{f} \tag{S3}$$

For calculating the eigenvalues and eigenvectors of the above system, we consider unforced system configuration, also called the modal equation, as follows,

$$\boldsymbol{M\ddot{x}} + \boldsymbol{Kx} = \boldsymbol{0} \tag{S4}$$

The natural frequencies and mode shapes of this system are calculated using the eigenvalues and eigenvectors of $\boldsymbol{M^{-1}K}$, and are expressed as follows,

$$f_{n1} = \frac{1}{2\pi}\sqrt{\frac{k_1+k_3}{2} + k_2 - \sqrt{\left(\frac{k_1-k_3}{2}\right)^2 + k_2^2}}, \sigma_{n1} = \sqrt{1+\left(\frac{k_1-k_3}{2k_2}\right)^2} - \frac{k_1-k_3}{2k_2} \tag{S5}$$

$$f_{n2} = \frac{1}{2\pi}\sqrt{\frac{k_1+k_3}{2} + k_2 + \sqrt{\left(\frac{k_1-k_3}{2}\right)^2 + k_2^2}}, \sigma_{n2} = -\sqrt{1+\left(\frac{k_1-k_3}{2k_2}\right)^2} - \frac{k_1-k_3}{2k_2} \tag{S6}$$

and the decoupled form of Eq. (S3) can be expressed as follows,

$$\begin{bmatrix} \sigma_{n1} & 1 \\ \sigma_{n2} & 1 \end{bmatrix} \begin{bmatrix} \ddot{y}_1 \\ \ddot{y}_2 \end{bmatrix} + \begin{bmatrix} f_{n1}^2 & 0 \\ 0 & f_{n2}^2 \end{bmatrix} \begin{bmatrix} \sigma_{n1} & 1 \\ \sigma_{n2} & 1 \end{bmatrix} \begin{bmatrix} y_1 \\ y_2 \end{bmatrix} = \begin{bmatrix} 0 \\ 0 \end{bmatrix} \tag{S7}$$

where f_{n1} and f_{n2} are the modal natural frequencies of the elastically coupled system, with $[\sigma_1, 1]^T$ and $[\sigma_2, 1]^T$, respectively, as the associated mode shapes of the considered system.

In the present study, two elastically-mounted tandem cylinders connected by an elastic coupling are subjected to $Re = 100$ free-stream flow and undergo flow-induced vibrations (FIV). Different values of spring stiffness, k_1, k_2, and k_3, result in the four cases shown in the inset, Case 1 ($k_2 = 0$): Elastically-mounted tandem cylinders; Case 2 ($k_3 = 0$): Elastically-mounted tandem cylinders with elastic coupling vibrating in-phase; and Case 3 ($k_3 = 0$): Elastically-mounted tandem cylinders with elastic coupling vibrating out-of-phase. In-phase and out-of-phase motions in the last two cases are devised by tuning natural mode frequencies with Strouhal frequency.

S5 Dynamic steady-state identification

As observed by Borazjani & Sotiropoulos (2009), the tandem cylinders may undergo a transformation in the flow regimes even after approximate steady state attainment. We have also observed this phenomenon for various tandem cylinder configurations, especially during transition of FIV regimes. For the same reason, we have considered the minimum simulation time of $t = 1200$, even if the signal seems to have attained a dynamically steady state. If the cylinder displacement signal shows signatures of a dynamically transient response, the simulations are continued till a dynamically steady state or stable quasi-periodic response is attained. As per our observation, the downstream cylinder response (A_2) is a better indicator of the dynamically steady state response. Some of the signals with the delayed dynamically steady state have been shown in Figure S3.

S6 Flow characteristics for stationary tandem cylinders

As discussed in §1.2, most past studies involving flow across rigid cylinders in tandem have reported flow structures, flow forces, Strouhal numbers, etc. However, studies by Alam (2016), at $Re = 200$,

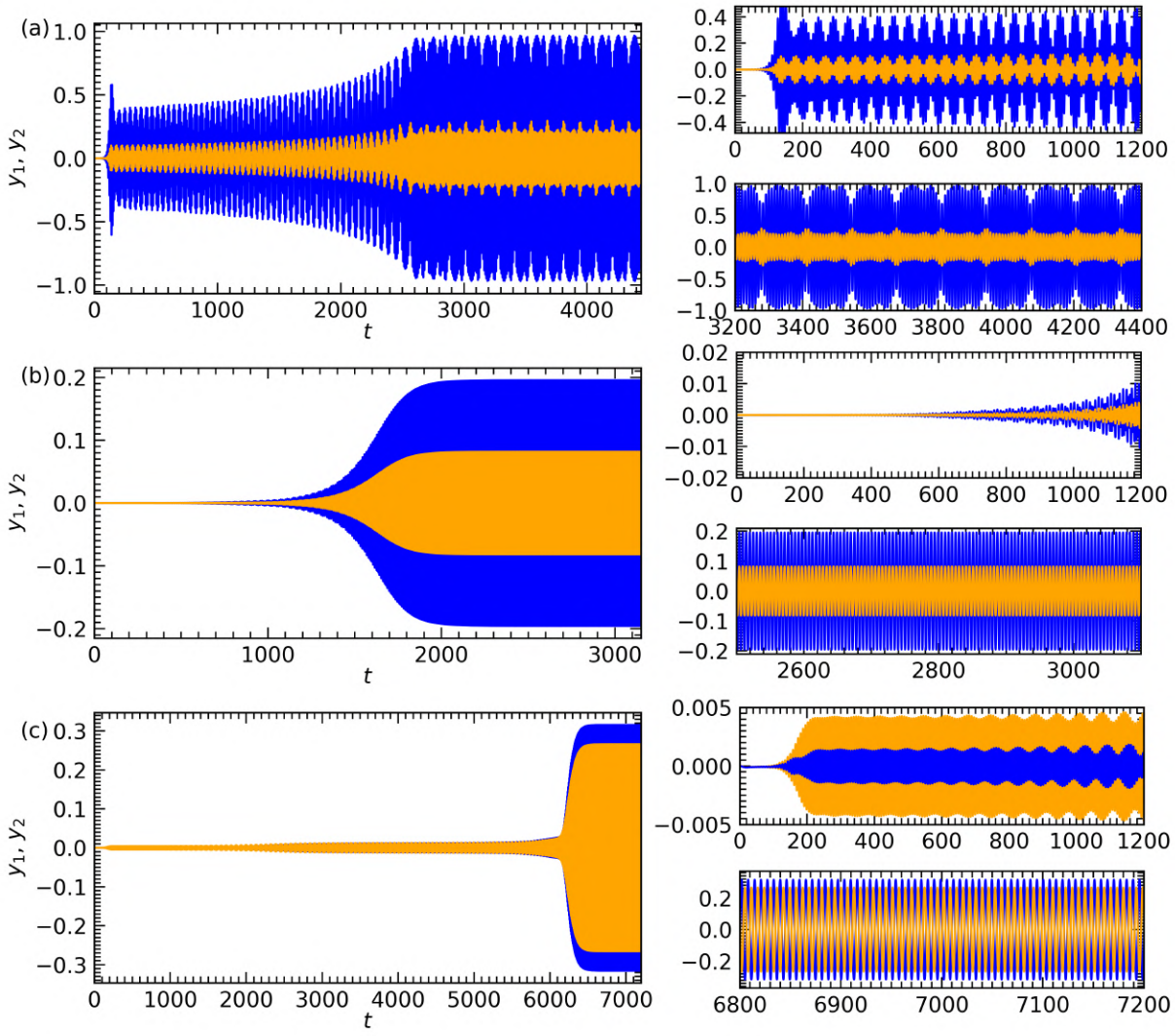

Figure S3: Transient displacements signals y_i for the tandem cylinders corresponding to (a) Case 1, $G = 4$, $U_R = 8.75$ (b) Case 2, $G = 3$, $U_R = 4.75$ and (c) Case 3, $G = 1.1$, $U_R = 5.75$. Panels on the right are the initial ($t \in [0, 1200]$) and final state of the transient signals.

indicate a dependence of lift magnitudes (C_{L1} and C_{L2}) on the phase difference between the forces acting on the two cylinders $\phi_{C_{L12}}$. Moreover, $\phi_{C_{L12}}$ will eventually influence the phase difference in the motion of the two cylinders ϕ_{y12}. Therefore, variation of flow forces (C_{Di} and C_{Li}), Strouhal frequency (St_{00}), and phase difference ($\phi_{C_{L12}}$) of stationary tandem cylinders, with G, is crucial for better quantification of the corresponding FIV results. We have calculated the relevant flow parameters for the stationary cylinders in tandem configuration for the present study at $Re = 100$ by varying $G \in [1.1, 6]$.

Figure S4(a) shows $\overline{C}_{D2} < 0$ for $G < 3.3$ with gradually decreasing $\overline{C}_{D1}$. This followed by a small region of $G \in [3.3, 4]$ with $\overline{C}_{D2}$ slightly positive. The negative mean drag at small G is also observed in past studies at low Re (Alam (2016)) as well as high Re (Zdravkovich (1977);

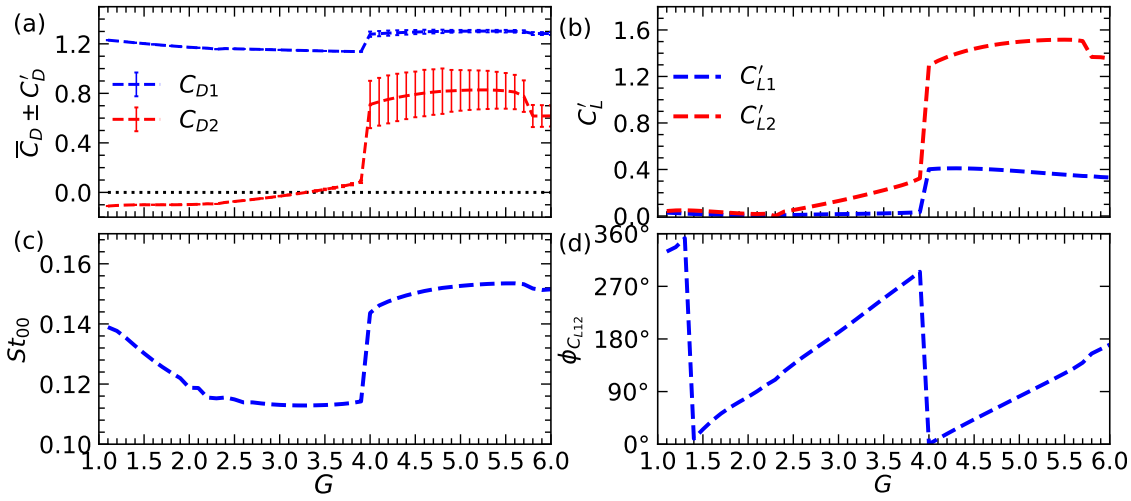

Figure S4: Flow characteristics of two tandem stationary cylinders as function of gap G between the cylinders (Case 0) (a) $\overline{C}_{D1}$ and $\overline{C}_{D2}$ with bars indicating C'_{D1} and C'_{D2}, (b) C'_{L1} and C'_{L2}, (c) St_{00}, and (d) $\phi_{C_{L12}}$.

Igarashi (1981); Alam *et al.* (2003)). C'_{D1}, C'_{D2} and C'_{L1} remain negligible for $G < 4$, with C'_{L2} gradually increasing from 0 to $\sim$ 0.3 for $G \in [2.3, 4]$. Interestingly, St_{00} decreases from 0.14 to 0.11 for $G < 2.3$, and then remains steady for $G \in [2.3, 4]$. $\phi_{C_{L12}}$ almost linearly increases with G, indicating an increasing time delay in vortices reaching from the upstream cylinder onto the downstream cylinder for larger G. All variables, $\overline{C}_{Di}$, C'_{Di}, C'_{Li}, St_{00} and $\phi_{C_{L12}}$, show sudden jumps at $G = 4$. Large C'_{D2} and C'_{L2} indicate strong incident vortices from the upstream cylinder. $St_{00} \sim 0.15$ for $G > 4$ indicates the tandem cylinder Strouhal frequency approaching isolated cylinder St_0. This corresponds to the critical gap ratio ($G_c = 4$) for vortex formation between the two tandem cylinders, and is consistent with studies by Mahir & Rockwell (1996); Carmo *et al.* (2010). Further, $\phi_{C_{L12}} \approx 0°$ (in-phase) at the critical gap ratio ($G_c = 4$) is consistent with previous studies by Sakamoto *et al.* (1987); Alam *et al.* (2003); Alam (2016). $\phi_{C_{L12}}$ shows a linear increment with G for $G > 4$ as well. Overall, the stationary tandem cylinder results show good agreement with the past literature, and these data will be used as a reference in subsequent sections.

S7 Variation of fluid flow forces

Figure S5(a) and (b) show the variation of maximum transverse force on the upstream (C'_{T1}) and downstream (C'_{T2}) cylinder, respectively, for Case 1. Similar to variation of A_1 described earlier, C'_{T1} signal (**??**(a)) in Case 1 ($G \geq 2$) closely resembles VIV characteristics of an isolated cylinder (Sharma *et al.* (2022*a*)). A narrow IB regime shows a sharp increase in C'_{T1}, followed by a gradual reduction in C'_{T1} in the UB lock-in regime. Interestingly, C'_{T1} reaches up to $\sim$ 2.0 ($G = 2$) in the IB regime, which is much larger than $\sim$ 1.0 observed for isolated cylinder VIV at $Re = 100$ (Sharma *et al.* (2022*a*)). The UB to LB regime transition results in a further sudden drop in C'_{T1}. The LB regime shows an almost stagnant C'_{T1}, with minor jumps near FD or WIV transition. The FD/WIV

regime shows $C'_{T1} \sim 0.05$ for $G = 2$ (FD), and $C'_{T1} \sim 0.3$ for $G \geq 3$ (WIV), implying a gap vortex formation at $G \geq 3$ for high U_R. $G = 1.1$ configuration also shows a VIV-like variation of C'_{T2} at low U_R. However, $G = 1.1$ exhibits $C'_{T1} \sim 0.5$ at high U_R, which is the largest among the considered gap ratios and is attributed to the galloping vibrations.

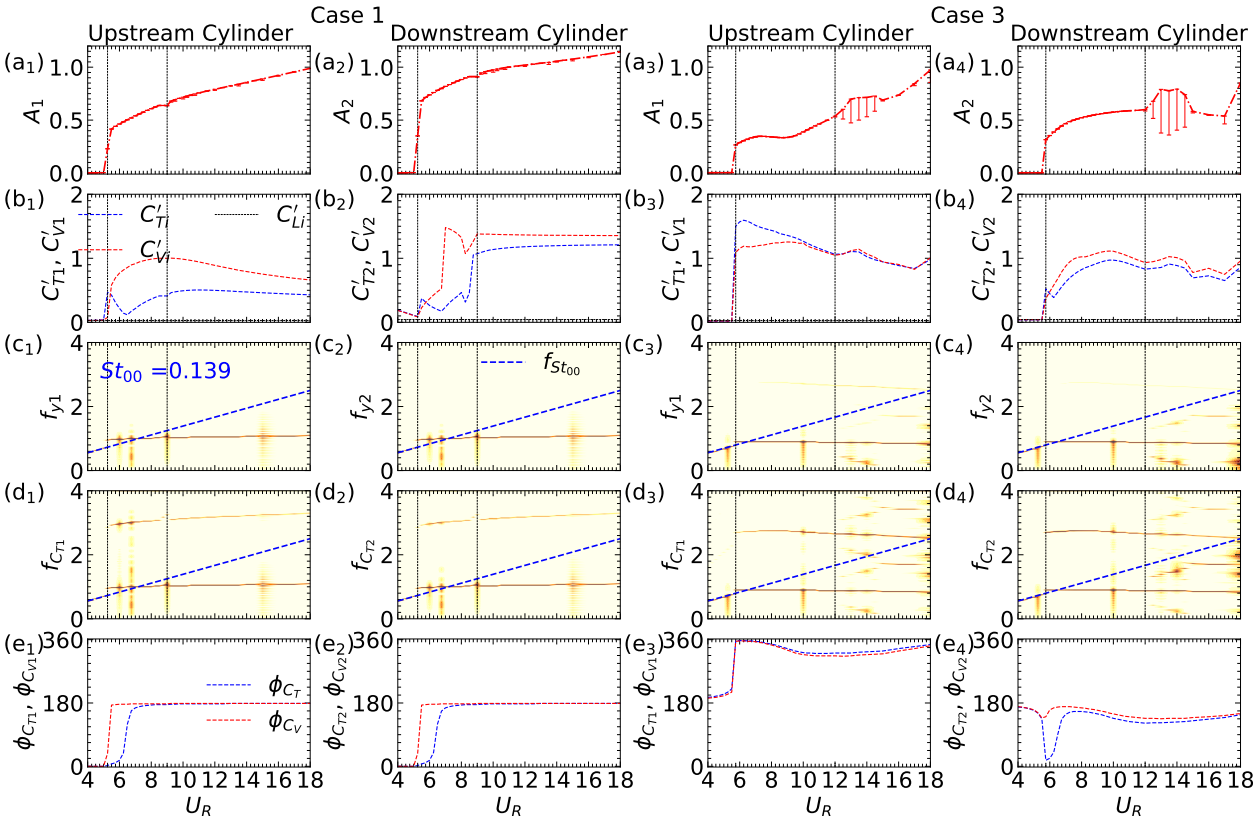

Figure S5: Variation of C'_{Ti} with reduced velocity U_R for upstream cylinder (left column) and downstream cylinder (right column) for Case 1 (a - b), Case 2 (c - d), and Case 3 (e - f). Difference cases of gap ratio G are compared in each panel.

The downstream cylinder shows a large C'_{T2} for a narrow IB regime. However, for $G \geq 3$, C'_{T2} remains very small throughout the UB and LB lock-in regime, followed by a rapid increase in C'_{T2} in the FD/WIV regime. A similar behavior is exhibited by the $G = 1.1$ system, irrespective of the stark differences in A_2 response. The only exception from this behavior is $G = 2$, indicating a larger C'_{T2} during UB (partial) and LB regimes.

The C'_{T1} and C'_{T2} variation for Case 2 (see Figure S5(c) and (d)) support the previous predictions of $A_1 \ll A_2$ in §4.2 due to differences in fluid flow forces. $C'_{T1} < C'_{T2}$ for $G \geq 3$ with individual variations qualitatively similar to the VIV system: C'_T is increasing during the IB regime, reducing during LN regime and nearly constant during FD regime. Like Case 1, C'_{T2} is significantly higher in the WIV regime ($G \geq 4$). While C'_{T2} is significantly lower in FD regime ($G < 4$), it is still higher than C_{T1}. $G = 1.1$ response is also similar to other low G FIV responses due to the absence of galloping in Case 2.

Figure S5(e) shows a sharp jump in C'_{T1} and C'_{T2} in MM regime ($G > 4$), and relatively much weaker jumps for ID regime of Case 3. Further, C'_{T1} and C'_{T2} attain an extra maxima (with cycle-

to-cycle fluctuations) at low U_R for $G \geq 4$, similar to A_1 and A_2. C'_{T1} drops from ~ 1.6 to ~ 0.35 during MM to LN transition, whereas the IB to LN transition shows a more gradual variation in C_{T1}. Interestingly, C'_{T2} becomes plateau at higher U_R and shows negligible sensitivity to U_R, especially for $G \geq 3$. This variation is a characteristic of the WIV regime (Assi *et al.* (2013)), in which the wake stiffness (constant for given Re) dominates over the structural stiffness and governs the FIV characteristics. No specific trend is seen in C_{T1} and C_{T2} signals, especially in the LN regime of Case 2 and 3 due to the elastic coupling (discussed in §5).

C'_{T1} shows some interesting features in Case 1 at extremely lower and higher U_R. For small U_R (ID regime), C'_{T1} remains ~ 0, up to $G = 5$. Similarly, at high U_R (regime 4), C'_{T1} reaches ~ 0.3 for $G \geq 3$ (WIV regime). As shown in §3, C'_{L1} reaches ~ 0.4 for stationary cylinders at $G \geq 4$ at $Re = 100$. This trend indicates that the stiffness domination suppresses (increases G_c) and inertia domination encourages (reduces G_c) the gap vortex formation between the tandem cylinders, even though A_1 is negligible (< 0.05) in those regimes.

S8 Variations in lock-in characteristics with G

This section presents the data of variation of transient FIV characteristics with G for Case 1 UB regime, Case 1 LB regime, Case 2 LN regime, and Case 3 LN regime. Further, those section shows the variation of DMD characteristics with G in the Case 1 UB regime.

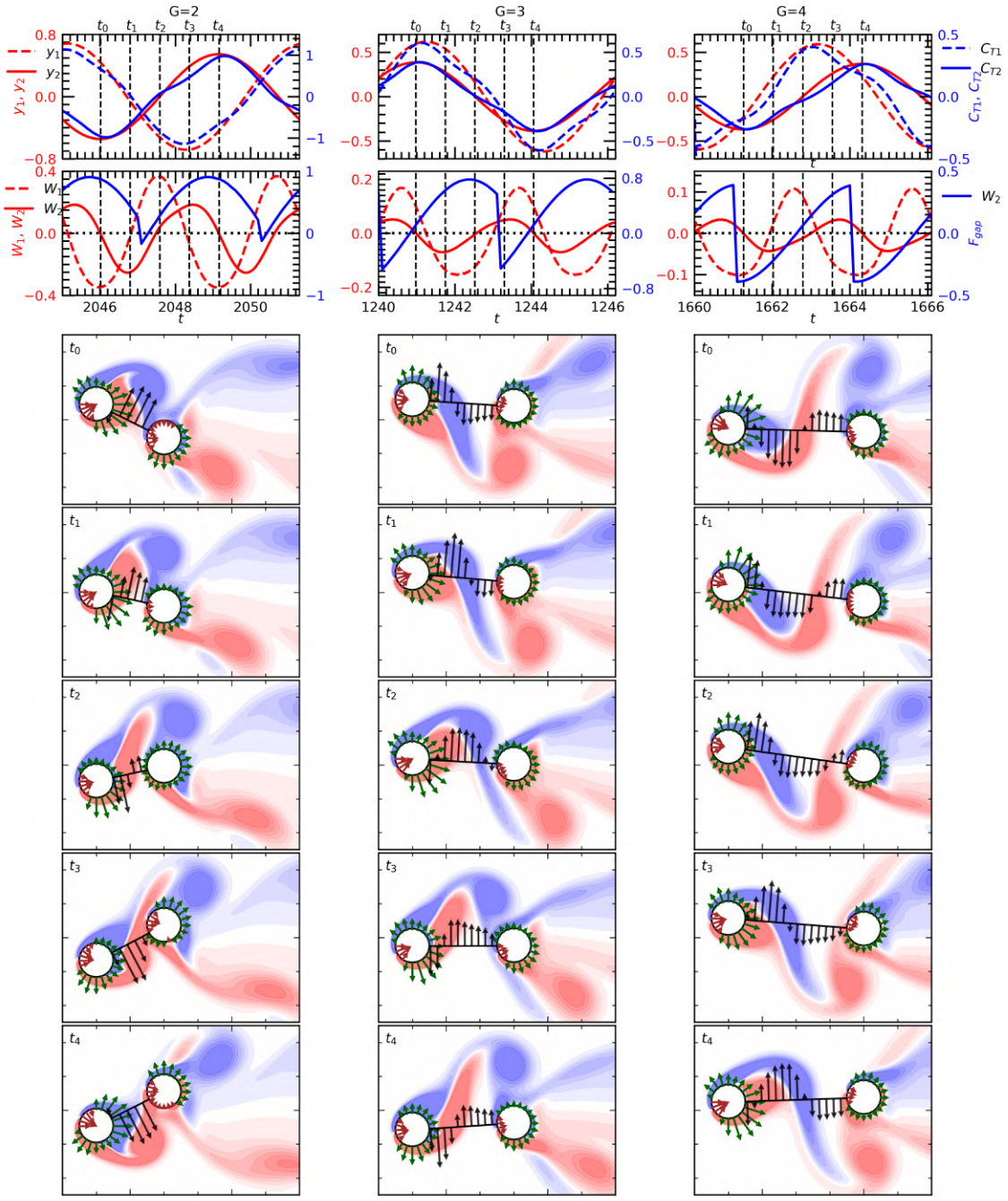

Figure S6: Transient FIV characteristics of Case 1 UB regime. First, second and third columns correspond to $G = 2$, 3, and 4, respectively. y_1, y_2, C_{T1}, and C_{T2} are plotted in first row. Transient variation of W_1, W_2 and F_g is plotted in the second row. Subfigures in rows 5 to 9 show the transient snapshots of near wake marked in the above signal plots. The black vectors on the line joining the cylinders indicate normal gap flow velocity c_g, and the arrows on the cylinder surface show the surface pressure variation.

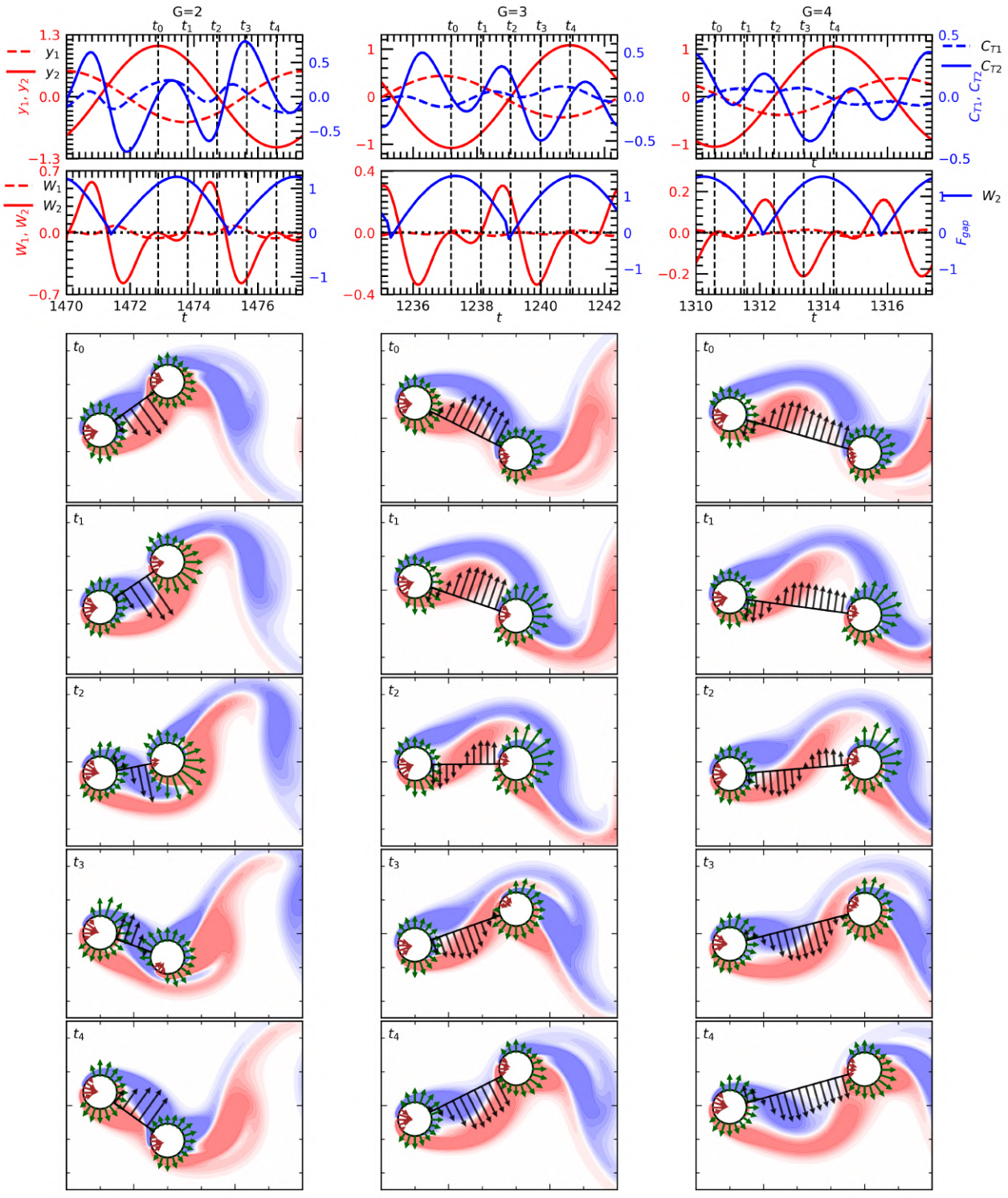

Figure S7: Transient FIV characteristics of Case 1 LB regime. Rest of the caption is same as Figure S6

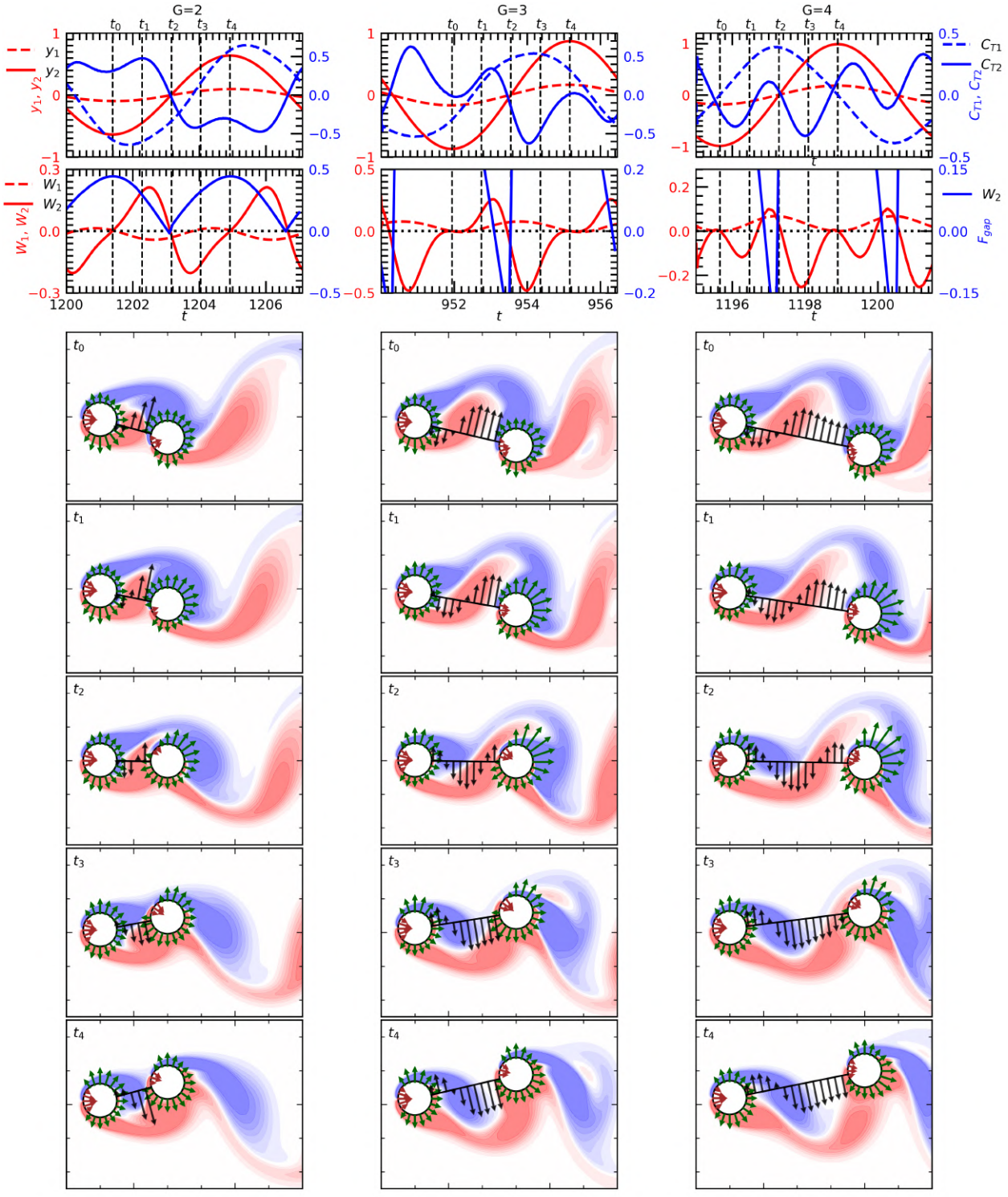

Figure S8: Transient FIV characteristics of Case 2 LN regime. Rest of the caption is same as Figure S6

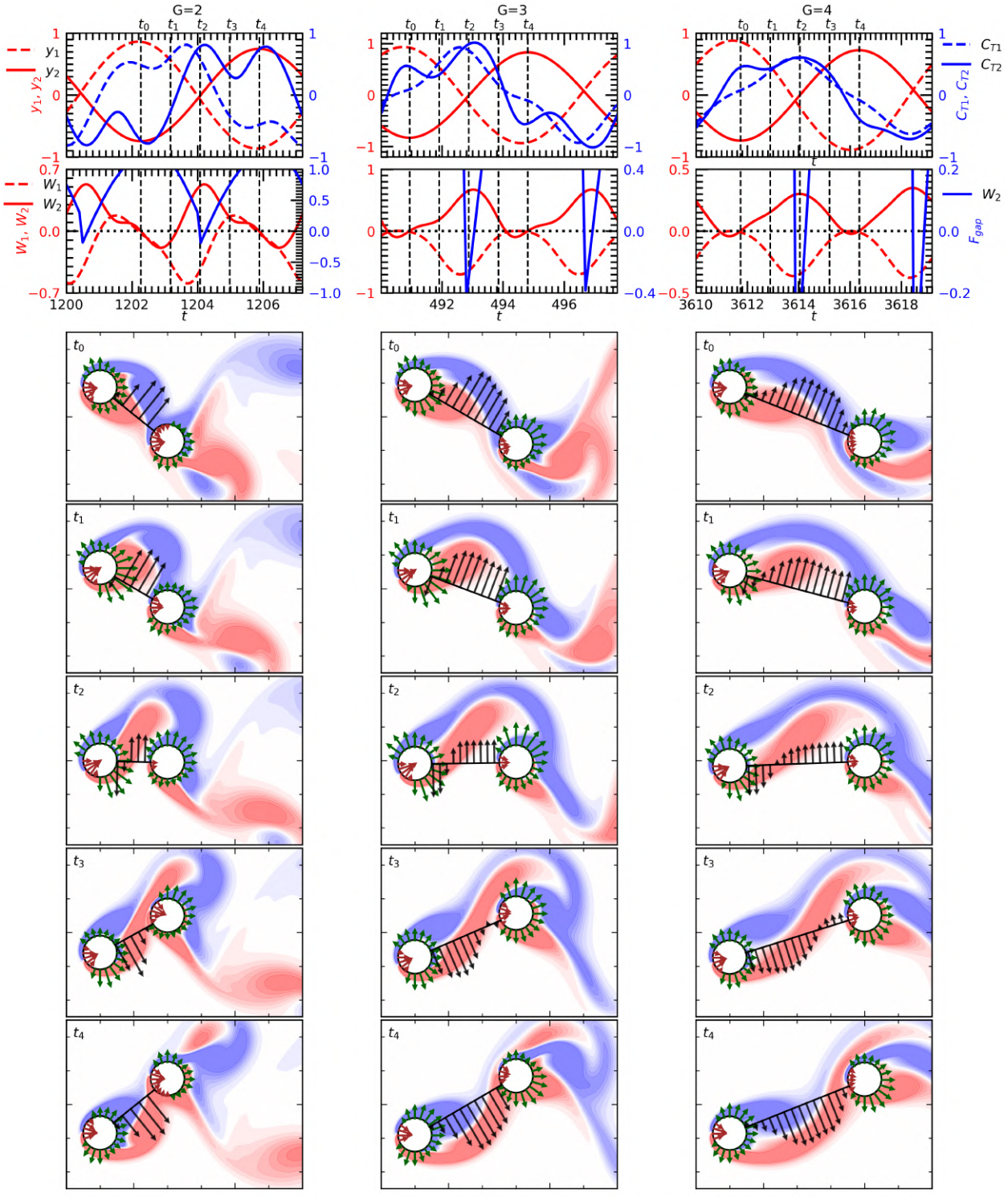

Figure S9: Transient FIV characteristics of Case 3 LB regime. Rest of the caption is same as Figure S6

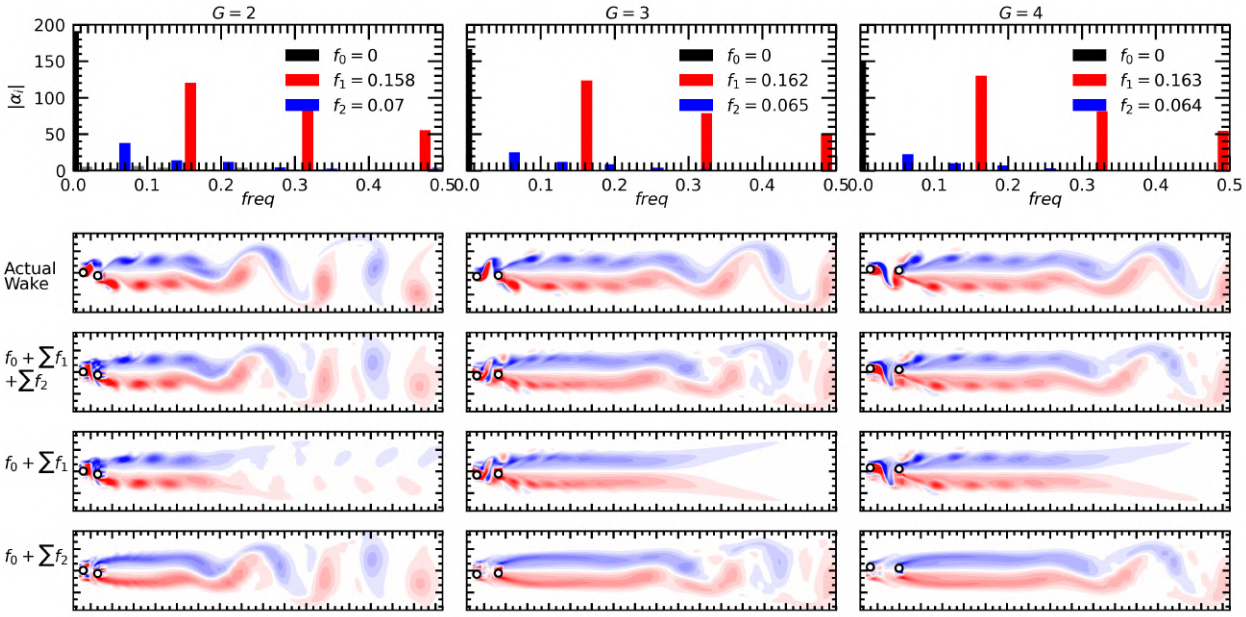

Figure S10: DMD characteristics for Case 1 UB regime. First, second and third columns correspond to $G = 1$, 2 and 3. First row plots the DMD amplitudes for the individual dominant frequencies present in the wake. Second row shows the actual wake, with third row showing the wake reconstructed using the considered DMD wake modes. The fourth and fifth row show the reconstructed wake for $f_0 + \sum f_1$ and $f_0 + \sum f_2$, respectively.

S9 Energy harvesting potential

As the present system does not include any structural damping or energy harvesting element, a direct estimation of the energy harvesting output cannot be estimated. However, assuming a small damping coefficient, we have quantified the mean power dissipated per unit reduced damping, for small damping coefficient values. This is based on the assumption that the damping coefficient is sufficiently small so that the FIV amplitude response of the damped system is nearly identical to the undamped system. The non-dimensional expression for mean power dissipated per unit of reduced damping is given as

$$\frac{\overline{P}_i}{c_i} = \frac{1}{T}\int_0^T \frac{P_i}{c_i} dt = \frac{1}{T}\int_0^T \frac{F_i \dot{y}_i}{c_i} dt = \frac{1}{T}\int_0^T (\dot{y}_i)^2 dt \tag{S8}$$

where $P_i = 2 * P_i^*/(\rho_f^* u_0^{*3} D^* L^*)$, $c_i = c_i^* D^*/m_s^* u_0^*$ and $T = T^* u_0^*/D^*$ are the non-dimensional power dissipation, reduced damping coefficient, and time period of FIV, respectively. The values $\dot{y}_1$, $\dot{y}_2$ and $\dot{y}_{12} = (\dot{y}_1 - \dot{y}_2)$ correspond to $\overline{P}_i/c_i$ of the energy harvesting system situated on the upstream, downstream, or between the cylinders, respectively.

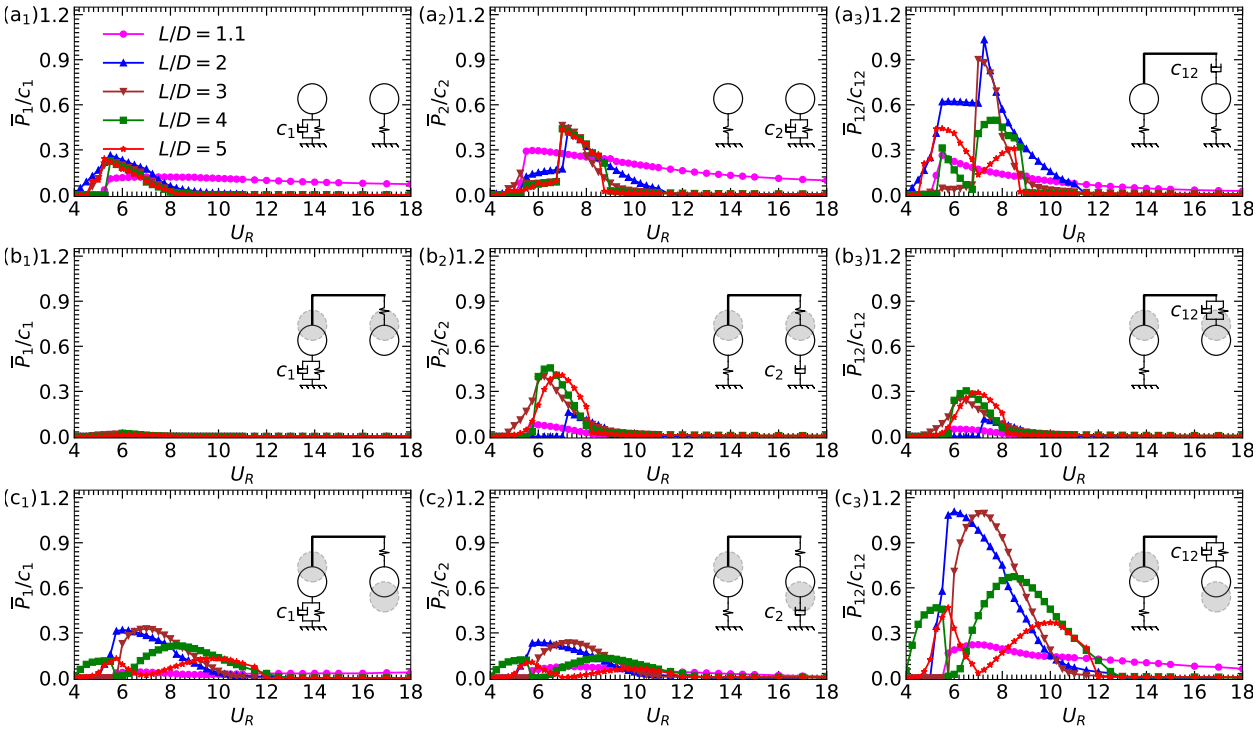

Figure S11: Non-dimensional average power per unit reduced damping for Case 1 (a_1-a_3), Case 2 (b_1-b_3) and Case 3 (c_1-c_3) for energy dissipation from the upstream (a_1-c_1), downstream (a_2-c_2) or between (a_3-c_3) the cylinders.

Figure S11 shows that the energy harvesting potential for $\overline{P}_{12}/c_{12}$ configuration is maximum for all three Cases ($\geq \overline{P}_1/c_1 + \overline{P}_2/c_2$). Further, among the three Cases considered, Case 3 shows maximum $\overline{P}_{12}/c_{12}$. Additionally, it is relatively difficult to realize a $\overline{P}_{12}/c_{12}$ configuration in Case

1 without introducing an intermediate stiffness between the cylinders, thus transforming them into Cases 2 or 3. Another point to be highlighted here is the fact that the Case 3 configuration utilizes a single energy harvesting unit, as compared to the two energy harvesting units utilized in the Case 1 counterpart, thus reducing the cost of energy generation.

S10 Computer animations

For a more detailed observation of the FIV response vortex shedding patterns of different regimes discussed in the §7, some additional computer animations are provided as follows:

1. ID regime for $G = 5$ of Case 1 at $U_R = 4$ (movie1.mp4).
2. IDG regime for $G = 5$ of Case 2 at $U_R = 4$ (movie2.mp4).
3. FD regime for $G = 2$ of Case 1 at $U_R = 18$ (movie3.mp4).
4. WIV regime for $G = 5$ of Case 1 at $U_R = 18$ (movie4.mp4).
5. UB regime for $G = 3$ of Case 1 at $U_R = 6$ (movie5.mp4).
6. LB regime for $G = 3$ of Case 1 at $U_R = 7.5$ (movie6.mp4).
7. LN regime for $G = 3$ of Case 2 at $U_R = 6.5$ (movie7.mp4).
8. LN regime for $G = 4$ of Case 3 at $U_R = 9$ (movie8.mp4).
9. GD regime for $G = 1.1$ of Case 1 at $U_R = 16$ (movie9.mp4).
10. GD regime for $G = 1.1$ of Case 3 at $U_R = 16$ (movie10.mp4).

The contour plots indicate vorticity variation, green/brown arrows represent negative/positive surface pressure on the cylinders' surface, and black arrows represent gap flow velocity along the line joining the two cylinders.

References

Alam, Md Mahbub 2016 Lift forces induced by phase lag between the vortex sheddings from two tandem bluff bodies. *Journal of Fluids and Structures* **65**, 217–237.

Alam, Md Mahbub, Moriya, Md, Takai, K & Sakamoto, H 2003 Fluctuating fluid forces acting on two circular cylinders in a tandem arrangement at a subcritical reynolds number. *Journal of Wind Engineering and Industrial Aerodynamics* **91** (1-2), 139–154.

Assi, GR da S, Bearman, Peter W, Carmo, Bruno Souza, Meneghini, Julio Romano, Sherwin, Spencer J & Willden, RHJ 2013 The role of wake stiffness on the wake-induced vibration of the downstream cylinder of a tandem pair. *Journal of Fluid Mechanics* **718**, 210–245.

Borazjani, Iman & Sotiropoulos, Fotis 2009 Vortex-induced vibrations of two cylinders in tandem arrangement in the proximity–wake interference region. *Journal of fluid mechanics* **621**, 321–364.

Carmo, BS, Meneghini, JR & Sherwin, SJ 2010 Possible states in the flow around two circular cylinders in tandem with separations in the vicinity of the drag inversion spacing. *Physics of Fluids* **22** (5), 054101.

Ding, Chenwei, Srinil, Narakorn, Bao, Yan, Zhou, Dai & Han, Zhaolong 2020 Vortex-induced vibrations of two mechanically coupled circular cylinders with asymmetrical stiffness in side-by-side arrangements. *Journal of Fluids and Structures* **95**, 102995.

Garg, Hemanshul, Soti, Atul K & Bhardwaj, Rajneesh 2018 A sharp interface immersed boundary method for vortex-induced vibration in the presence of thermal buoyancy. *Physics of Fluids* **30** (2), 023603.

Garg, Hemanshul, Soti, Atul Kumar & Bhardwaj, Rajneesh 2020 Thermal buoyancy induced suppression of wake-induced vibration. *International Communications in Heat and Mass Transfer* **118**, 104790.

Igarashi, Tamotsu 1981 Characteristics of the flow around two circular cylinders arranged in tandem: 1st report. *Bulletin of JSME* **24** (188), 323–331.

Mahir, NECATİ & Rockwell, D 1996 Vortex formation from a forced system of two cylinders. part i: Tandem arrangement. *Journal of Fluids and Structures* **10** (5), 473–489.

Mittal, R., Dong, H., Bozkurttas, M., Najjar, F. M., Vargas, A. & von Loebbecke, A. 2008 A versatile sharp interface immersed boundary method for incompressible flows with complex boundaries. *Journal of Computational Physics* **227** (10), 4825–4852.

Sakamoto, H, Hainu, H & Obata, Y 1987 Fluctuating forces acting on two square prisms in a tandem arrangement. *Journal of Wind Engineering and Industrial Aerodynamics* **26** (1), 85–103.

Seo, Jung Hee & Mittal, Rajat 2011 A sharp-interface immersed boundary method with improved mass conservation and reduced spurious pressure oscillations. *Journal of Computational Physics* **230** (19), 7347–7363.

Sharma, Gaurav, Garg, Hemanshul & Bhardwaj, Rajneesh 2022*a* Flow-induced vibrations of elastically-mounted c-and d-section cylinders. *Journal of Fluids and Structures* **109**, 103501.

Sharma, Gaurav, Pandey, Avinash Kumar & Bhardwaj, Rajneesh 2022*b* Effect of shape of frontbody and afterbody on flow past a stationary cylinder at re= 100. *Physics of Fluids* .

Zdravkovich, M. M. 1977 Review of Flow Interference Between Two Circular Cylinders in Various Arrangements. *Journal of Fluids Engineering* **99** (4), 618–633.